Engineering the electronic and optical properties of the zigzag MoS₂/WS₂ heterostructure nanotubes

R. Huang, Y. Z. Wang[*], C. B. Li, Z. W. Li, C. Dang
Faculty of Mathematics and Physics, Huaiyin Institute of Technology, Jiangsu, 223003, China

The electronic structures and optical properties of zigzag MoS_2/WS_2 heterostructure nanotubes (NTs) with different component ratio and uniaxial strain have been investigated by using first-principles calculations. The band gap of the zigzag MoS_2/WS_2 heterostructure NTs remains the direct band gap with different ratio of WS_2 and uniaxial strain. while the band gap of which increases obviously with the increase of WS_2 when the ratio is more than half. Moreover, the band gap of the zigzag MoS_2/WS_2 heterostructure NT decreases linearly with the increase of tensile strain, while the band gap of which increases firstly and then decreases with the increase of compressive strain. The dielectric spectra occur blue shift with the increase of component ratio of WS_2. The static dielectric constants decrease monotonously with the increase of the ratio of WS_2. Interestingly, the dielectric spectra for parallel and perpendicular to the tube axis exhibit opposite shift under the same strain. The static dielectric constants of which also show the different variation tendency under the same strain. These results suggest that the zigzag MoS_2/WS_2 heterostructure NTs can be promising candidates for optoelectronic applications.

1. Introduction

Since the synthesis of WS_2 NTs in 1992[1], the transition metal dichalcogenide (TMD) (MX_2, M=Mo, W, etc.; X=S, Se, etc.) NTs have attracted extensive attention due to their outstanding physical and chemical properties[2-5]. Among them, the MoS_2 NTs and WS_2 NTs have gained increasing attention due to their potential applications in the optoelectronic device[6-8], catalysis[9], transistors and batteries[10, 11]. Furthermore, to modulate the electronic and optical properties for the future applications in the optoelectronic nanodevices, various strategies have been developed, such as strain[12, 13], electric field[4], and so on.

Recently, to make full use of the unique properties of the two-dimensional (2D) TMD, 2D TMD heterostructures (MoS_2/WS_2, MoS_2/MoS_2, $MoSe_2/WSe_2$, WSe_2/MoS_2, $ReSe_2/MoS_2$, WS_2/SnS_2, etc.) have received considerable research owing to their diverse applications, such as photodetectors[14, 15], sensors[16, 17], transistors[18], Li-ion batteries[19] and solar cells[20]. Among them, MoS_2/WS_2 lateral heterostructures have received more attention. Gong et al. have

prepared the WS_2/MoS_2 vertical and lateral heterostructures under different vapor phase growth temperatures[21]. Bogaert et al. have synthesized the MoS_2/WS_2 lateral heterostructures via two-step chemical vapor deposition[22]. Berweger et al. have studied the spatial photoconductivity distribution and long-term carrier accumulation in MoS_2/WS_2 lateral heterostructures[23]. Zhu et al. have realized the selective growth of large WS_2/MoS_2 lateral and vertical heterostructures by hydroxide-assisted nucleation in a one-pot strategy, and the synthesized large (~1 mm) lateral heterostructures exhibit excellent electronic properties[24]. Considering the TMD heterostructure NTs can be fabricated by wrapping their monolayer. In our previous work, we have studied the electronic and optical properties of the chalcogen-changing $MoS_2/MoSe_2$ heterostructure NTs[25]. However, strain-tunable electronic and optical properties of metal-changing MoS_2/WS_2 heterostructure NTs have not been systematically investigated so far.

In this paper, we systematically studied the electronic structures and optical properties of the zigzag MoS_2/WS_2 heterostructure NTs with different component ratio of WS_2 and uniaxial strain based on first-principles calculations. It is found that the band gap, dielectric function and static dielectric constants of the zigzag MoS_2/WS_2 heterostructure NTs can be modulated with different component ratio of WS_2 and uniaxial strain.
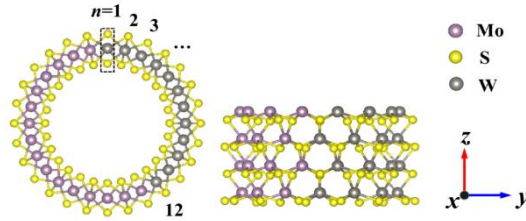
Fig. 1. The top and side view of the optimized (14, 0) $(MoS_2)_{(28-n)}/(WS_2)_n$ (n=12) heterostructure NT.

2. Computational methods

The calculations based on the density functional theory (DFT) with projector augmented wave (PAW) potential basis are performed in Vienna ab initio simulation package (VASP)[26-28]. The exchange-correlation potential is described by the generalized gradient approximation (GGA) of the Perdew-Burke-Ernzerhof (PBE) parametrization[29]. The plane-wave cutoff energy is set to be 500 eV. The lattice constants and internal atomic positions are fully relaxed until the atomic forces are smaller than 0.01 eV/Å, and the convergence criterion of energy is set to 10^{-5} eV. A k-point mesh of $1\times1\times11$ is used to sample the Brillouin zone. To avoid the interaction between adjacent images, the vacuum region is more than 15 Å in the x and y directions. In this work, (14, 0) $(MoS_2)_{(28-n)}/(WS_2)_n$ heterostructure NTs are constructed, as shown in Fig. 1, where n represents the number of $W-S_2$ in the unit cell of the NT.

In order to investigate the optical properties, the complex dielectric function $\varepsilon(\omega) = \varepsilon_1(\omega) + i\varepsilon_2(\omega)$ is computed, where the imaginary $\varepsilon_2(\omega)$ can be obtained by the following formula[30]:

$$\varepsilon_2 = \frac{4\pi^2 e^2}{\Omega}\lim_{q\to0}\frac{1}{q^2}\sum_{c,v,k}2\omega_k\delta(\varepsilon_{ck}-\varepsilon_{vk}-\omega)\times\langle u_{ck}+e_{\alpha q}|u_{vk}\rangle\langle u_{ck}+e_{\beta q}|u_{vk}\rangle^* \tag{1}$$

where the indices c and v present conduction and valence band states, respectively, and u_{ck} is the cell periodic part of the orbitals at the k-points.

The real part $\varepsilon_1(\omega)$ can be obtained from $\varepsilon_2(\omega)$ by the Kramers-Kronig relation:

$$\varepsilon_1(\omega) = 1 + \frac{2}{\pi} P \int_0^\infty \frac{\varepsilon_2^{\alpha\beta}(\omega')\omega'}{\omega'^2 - \omega^2 + i\eta} d\omega' \tag{2}$$

where P stands the principle value of the integral and η is an infinitesimal number denotes complex shift.
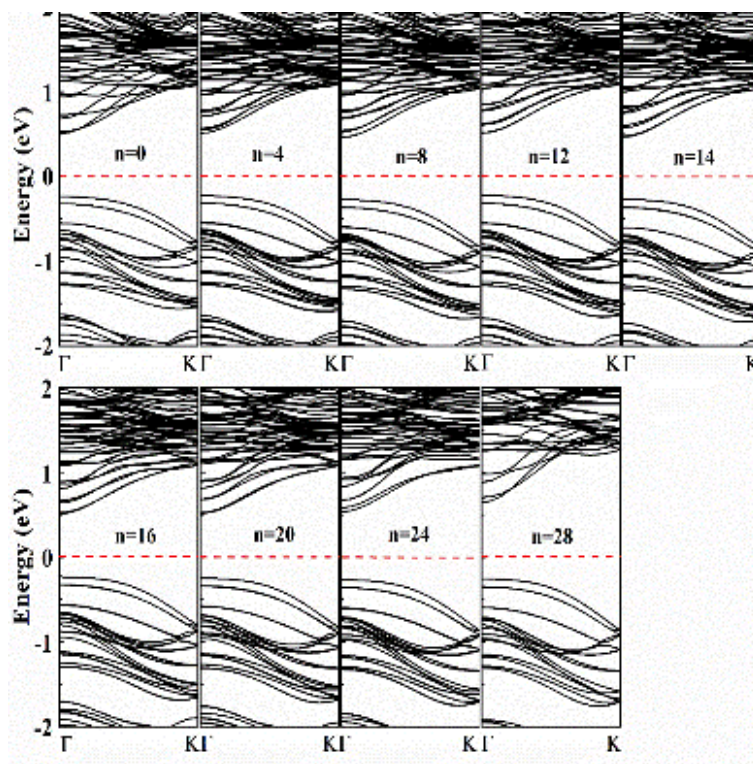
Fig. 2. The energy band structures of (14, 0) $(MoS_2)_{(28-n)}/(WS_2)_n$ NTs.
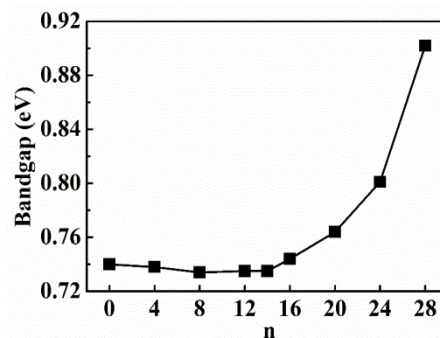
Fig. 3. Band gap variation of (14, 0) $(MoS_2)_{(28-n)}/(WS_2)_n$ NTs with n.
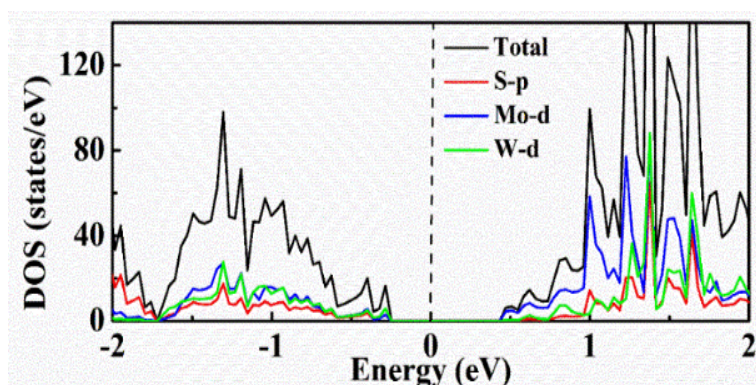
Fig. 4. The total and projected density of states of (14, 0) (MoS$_2$)$_{14}$/(WS$_2$)$_{14}$ heterostructure NTs.

3. Results and discussion

The calculated band structures of (14, 0) (MoS$_2$)$_{(28-n)}$/(WS$_2$)$_n$ heterostructure NTs are shown in Fig. 2. As shown in Fig. 2, the (14, 0) (MoS$_2$)$_{(20-n)}$/(WS$_2$)$_n$ (n= 4, 8, 12, 14, 16, 20, 24) heterostructure NTs retain the direct bang gap, which are consistent with that of (14, 0) MoS$_2$ (n=0) and (14, 0) WS$_2$ (n=28) NTs. The band gap of the (14, 0) MoS$_2$ is 0.74 eV, which is consistent with the previous reports[31]. The calculated band gap of the (14, 0) (MoS$_2$)$_{(28-n)}$/(WS$_2$)$_n$ NTs as a function of n is shown in Fig. 3. It can be seen that the variation of band gap is small when the n is less than or equal 14 for the (14, 0) (MoS$_2$)$_{(28-n)}$/(WS$_2$)$_n$ NTs, while the variation of which is obvious when the ratio of WS$_2$ is more than half. The smallest band gap is 0.73 eV for (14, 0) (MoS$_2$)$_{14}$/(WS$_2$)$_{14}$ heterostructure NT. To further understand the electronic properties of MoS$_2$/WS$_2$ heterostructure NTs, we illustrate the total and projected density of states of (14, 0) (MoS$_2$)$_{14}$/(WS$_2$)$_{14}$ heterostructure NT in Fig. 4. It can be seen that the valence band maximum (VBM) is mainly composed of *d* orbitals of both Mo and W atoms and the *p* orbital of the S atoms, the conduction band minimum (CBM) is mainly contributed by the *d* orbital of the Mo atoms.
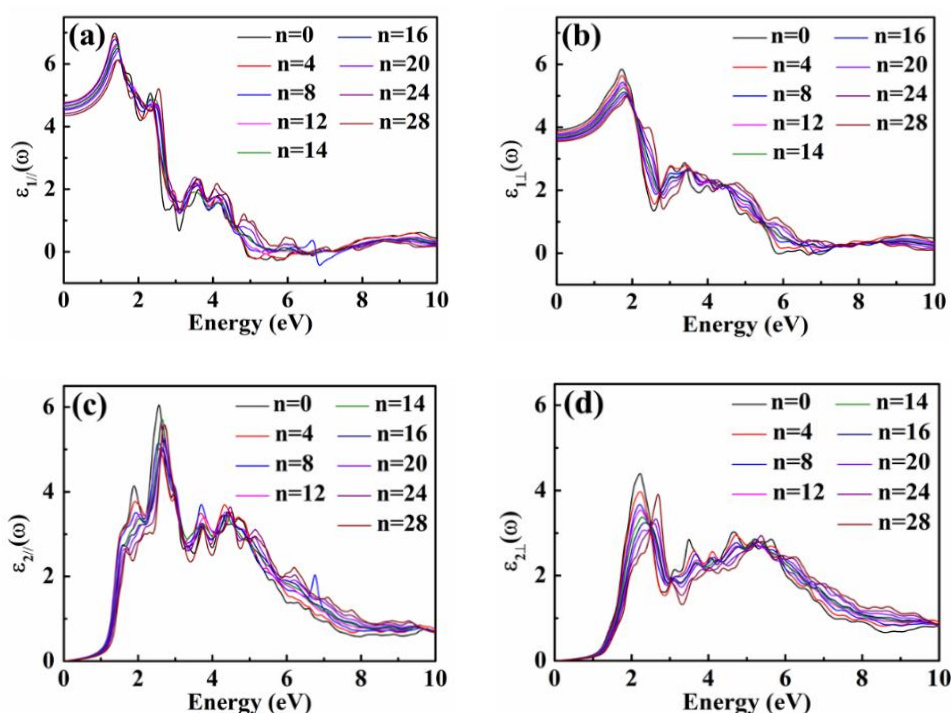
Fig. 5. Calculated real part $\varepsilon_1(\omega)$ and imaginary part $\varepsilon_2(\omega)$ of the dielectric function of (14, 0)

$(MoS_2)_{(28-n)}/(WS_2)_n$ NTs.
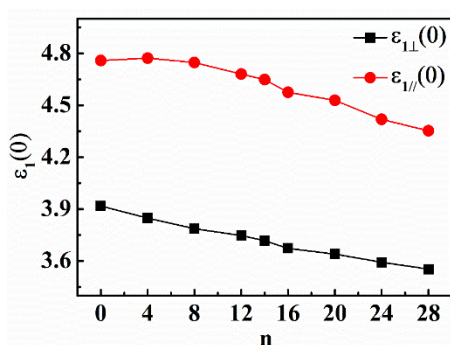
Fig. 6. Calculated static dielectric constants $\varepsilon_1(0)$ of (14, 0) $(MoS_2)_{(28-n)}/(WS_2)_n$ NTs.

For the promising photoelectronic applications of MoS_2/WS_2 heterostructure NTs, the optical properties of which have been studied based on the dielectric function. The real part $\varepsilon_1(\omega)$ and imaginary part $\varepsilon_2(\omega)$ of complex dielectric function for parallel (//) (along z direction) and perpendicular ($\perp$) (average of x and y direction) to the tube axis are calculated. The calculated the real part and imaginary for parallel and perpendicular to the tube axis of (14, 0) $(MoS_2)_{(28-n)}/(WS_2)_n$ NTs are shown in Fig. 5. It can be seen the dielectric function is anisotropic. The main peaks are found in the low energy range from 1 to 3 eV, which indicates that these NTs show a strong absorption in the visible and near-IR region. Especially, the dielectric spectra show the blue shift with the increase of the ratio of WS_2 for the MoS_2/WS_2 heterostructure NTs. We also find the change of the dielectric spectra of MoS_2/WS_2 heterostructure NTs is only that between pristine MoS_2 NT and pristine WS_2 NT. This indicates we can realize different optical response of TM heterostructure NT by choosing different pristine materials. The calculated static dielectric

constants $\varepsilon_1(0)$ ($\omega=0$) of the MoS_2/WS_2 NTs are shown in Fig. 6. It can be seen that the static dielectric constants for parallel to the tube axis are larger than that for perpendicular to the tube axis, and all the static dielectric constants decrease with the increase of the ratio of WS_2.
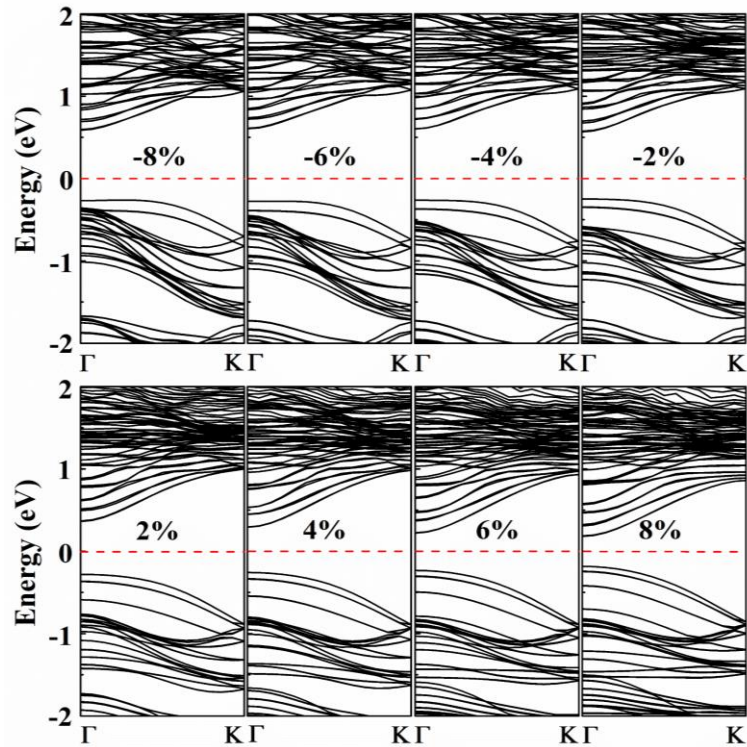
Fig. 7. Calculated band structures of (14, 0) $(MoS_2)_{14}/(WS_2)_{14}$ NTs under uniaxial strain.
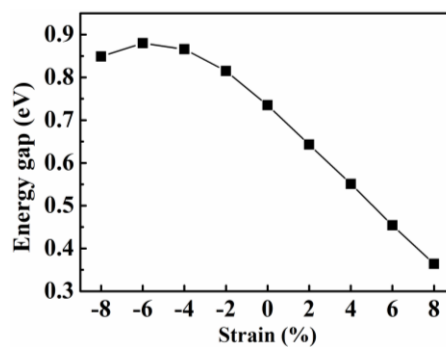
Fig. 8. Uniaxial strain dependence of energy gap of (14, 0) $(MoS_2)_{14}/(WS_2)_{14}$ NTs.
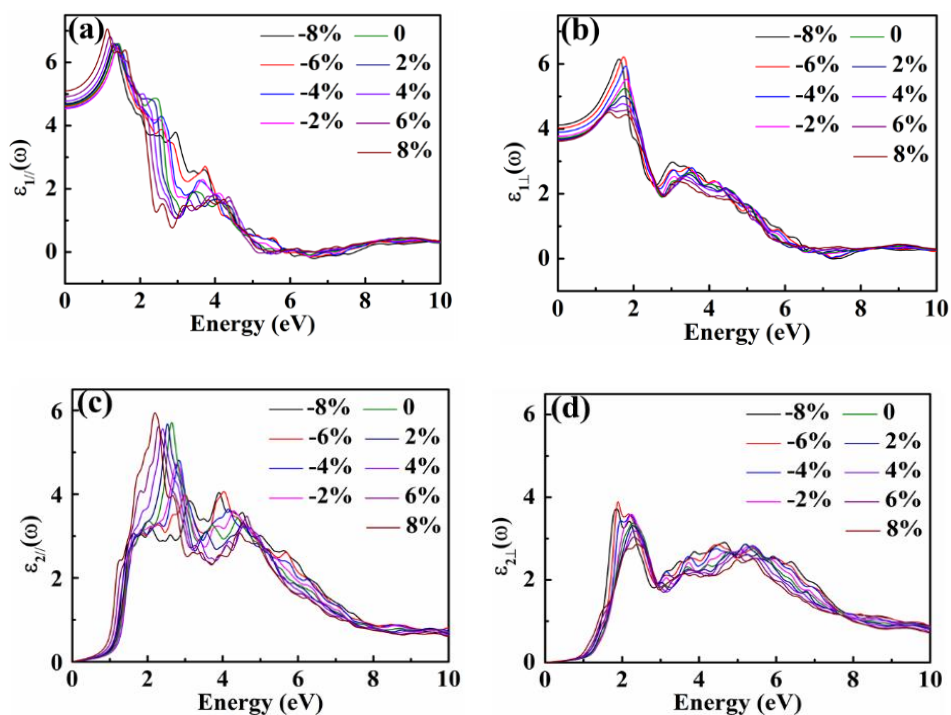
Fig. 9. Calculated real part $\varepsilon_1(\omega)$ and imaginary part $\varepsilon_2(\omega)$ of the dielectric function of (14, 0) $(MoS_2)_{14}/(WS_2)_{14}$ NTs under uniaxial strain.
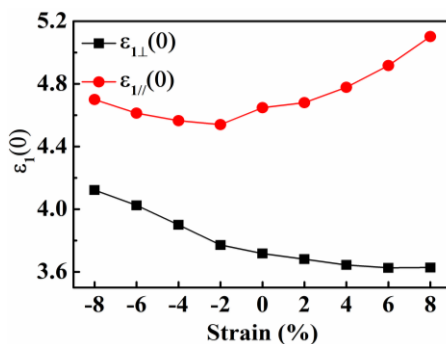
Fig. 10. Calculated static dielectric constant $\varepsilon_1(0)$ of (14, 0) $(MoS_2)_{14}/(WS_2)_{14}$ NTs under uniaxial strain.

In order to investigate the strain effect on the electronic and optical properties of zigzag MoS_2/WS_2 heterostructure NTs, we study the (14, 0) $(MoS_2)_{14}/(WS_2)_{14}$ NT as a representative model. Fig. 7 shows the calculated band structures of (14, 0) $(MoS_2)_{14}/(WS_2)_{14}$ heterostructure NT under different uniaxial strain. It can be seen that the band gap is significantly influenced by the uniaxial strain, but it remains direct band gap. Fig. 8 shows the variation of the band gap with different uniaxial strain. As shown in Fig. 8, the band gap decreases linearly with the increase of tensile strain, which can be decreased to 50% under 8% tensile strain. While the band gap increases firstly and then decreases with the increase of compressive strain. Fig. 9 shows the

calculated real part $\varepsilon_1(\omega)$ and imaginary part $\varepsilon_2(\omega)$ of the dielectric function of (14, 0) $(MoS_2)_{14}/(WS_2)_{14}$ NT under different uniaxial strain. Under uniaxial strain, all dielectric spectra are similar, but the main peaks shift obviously with the different strain. The dielectric spectra for parallel to the tube axis occur red shift with the strain range from -8% to 8%, while the dielectric spectra for perpendicular to the tube axis exhibit blue shift with the same strain. Fig. 10 shows the calculated static dielectric constant $\varepsilon_1(0)$ of (14, 0) $(MoS_2)_{14}/(WS_2)_{14}$ NT with different uniaxial strain. The static dielectric constant for parallel to the tube axis decreases monotonously with the strain range from -8% to 8%. While the static dielectric constant for perpendicular to the tube axis increases under tensile strain. The different variation tendency of the dielectric spectra and the static dielectric constants maybe due to the different structure variation in two directions under the uniaxial strain.

4. Conclusions

In summary, first-principles calculations have been used to study the electronic structures and optical properties of zigzag MoS_2/WS_2 heterostructure NTs with different component ratios and uniaxial strain. The results show that the zigzag MoS_2/WS_2 heterostructure NTs remain the direct band gap with different ratio of WS_2 and uniaxial strain. And the band gap of which increases obviously when the ratios are more than half. Moreover, the band gap of the zigzag MoS_2/WS_2 heterostructure NTs decreases linearly with the increase of tensile strain, while the band gap of which increases firstly and then decreases with the increase of compressive strain. At the same time, the dielectric spectra occur blue shift with the increase of component ratio of WS_2. The static dielectric constants decrease monotonously with the increase of the ratios of WS_2. Interestingly, the dielectric spectra of parallel and perpendicular to the tube axis exhibit opposite shift under the same strain. The static dielectric constants of parallel and perpendicular to the tube axis also show the different variation tendency under the same strain. Our results exhibit the electronic and optical properties of MoS_2/WS_2 heterostructure NTs can be tuned by different WS_2 ratio and strain, which suggest that the zigzag MoS_2/WS_2 heterostructure NTs can be promising candidates for optoelectronic applications.

Acknowledgements

References

[1] R. Tenne, L. Margulis, M. Genut, G. Hodes, Nature **360**, 444 (1992).
[2] L. Kang, W. B. Zhang, F. Zhou, B. Y. Tang, J. Phys. D: Appl. Phys. **49**, 185301 (2016).

[3] X. Q. Wang, B. J. Zheng, B. Wang, H. Q. Wang, B. C. Sun, J. R. He, W. L. Zhang, Y. F. Chen, Electrochim. Acta **299**, 197 (2019).

[4] N. Zibouche, P. Philipsen, A. Kuc, J. Phys. Chem. C **123**, 3892 (2019).

[5] K. R. O'Neal, J. G. Cherian, A. Zak, R. Tenne, Z. Liu, J. L. Musfeldt, Nano Lett. **16**, 993 (2015).

[6] J. P. Mathew, G. Jegannathan, S. Grover, P. D. Dongare, R. D. Bapat, B. A. Chalke, S. C. Purandare, M. M. Deshmukh, Appl. Phys. Lett. **105**, 223502 (2014).

[7] J. H. Mokkath, Chem. Phys. Lett. **706**, 641 (2018).

[8] D. R. Kazanov, A. V. Poshakinskiy, V. Y. Davydov, A. N. Smirnov, I. A. Eliseyev, D. A. Kirilenko, M. Remskar, S. Fathipour, A. Mintairov, A. Seabaugh, B. Gil, T. V. Shubina, Appl. Phys. Lett. **113**, 101106 (2018).

[9] K. Xu, F. M. Wang, Z. X. Wang, X. Y. Zhan, Q. S. Wang, Z. Z. Cheng, M. Safdar, J. He, ACS Nano **8**, 8468 (2014).

[10] M. Strojnik, A. Kovic, A. Mrzel, J. Buh, J. Strle, D. Mihailovic, AIP Adv. **4**, 097114 (2014).

[11] G. D. Li, X. Y. Zeng, T. D. Zhang, W. Y. Ma, W. P. Li, M. Wang, CrystEngComm **16**, 10754 (2014).

[12] W. F. Li, G. Zhang, M. Guo, Y. W. Zhang, Nano Res. **7**, 518 (2014).

[13] Y. Z. Wang, R. Huang, B. L. Gao, G. Hu, F. Liang, Y. L. Ma, Chalcogenide Lett. **15**, 535 (2018).

[14] T. H. Tsai, Z. Y. Liang, Y. C. Lin, C. C. Wang, K. I. Lin, K. Suenaga, P. W. Chiu, ACS Nano **14**, 4559 (2020).

[15] Y. F. Pei, R. Chen, H. Xu, D. He, C. Z. Jiang, W. Q. Li, X. H. Xiao, Nano Res. **14**, 1819 (2021).

[16] W. H. Wu, Q. Zhang, X. Zhou, L. Li, J. W. Su, F. K. Wang, T. Y. Zhai, Nano Energy **51**, 45 (2018).

[17] M. Schleicher, M. Fyta, ACS Appl. Electron. Mater. **2**, 74 (2020).

[18] Y. Z. Xue, Y. P. Zhang, Y. Liu, H. T. Liu, J. C. Song, J. Sophia, J. Y. Liu, Z. Q. Xu, Q. Y. Xu, Z. Y. Wang, J. L. Zheng, Y. Q. Liu, S. J. Li, Q. L. Bao, ACS Nano **10**, 573 (2016).

[19] D. Wang, L. M. Liu, S. J. Zhao, Z. Y. Hu, H. Liu, J. Phys. Chem. C **120**, 4779 (2016).

[20] L. Wang, M. Tahir, H. Chen, J. B. Sambur, Nano Lett. **19**, 9084 (2019).

[21] Y. J. Gong, J. H. Lin, X. L. Wang, G. Shi, S. D. Lei, Z. Liu, X. L. Zou, G. L. Ye, R. Vajtai, B. I. Yakobson, H. Terrones, M. Terrones, B. K. Tay, J. Lou, S. T. Pantelides, Z. Liu, W. Zhou, P. M. Ajayan, Nat. Mater. **13**, 1135 (2014).

[22] K. Bogaert, S. Liu, J. Chesin, D. Titow, S. Gradečak, S. Garaj, Nano Lett. **16**, 5129 (2016).

[23] S. Berweger, H. Y. Zhang, P. K. Sahoo, B. M. Kupp, J. L. Blackburn, E. M. Miller, T. M. Wallis, D. V. Voronine, P. Kabos, S. U. Nanayakkara, ACS Nano **14**, 14080 (2020).

[24] J. T. Zhu, W. Li, R. Huang, L. Ma, H. M. Sun, J. H. Choi, L. Q. Zhang, Y. Cui, G. F. Zou, J. Am. Chem. Soc. **142**, 16276 (2020).

[25] Y. Z. Wang, R. Huang, F. J. Kong, B. L. Gao, G. N. Li, F. Liang, G. Hu, Superlattice Microst. **132**, 106156 (2019).

[26] P. E. Blöchl, Phys. Rev. B **50**, 17953 (1994).

[27] G. Kresse, J. Furthmüller, Comp. Mater. Sci. **6**, 15 (1996).

[28] G. Kresse, J. Furthmüller, Phys. Rev. B **54**, 11169 (1996).

[29] J. P. Perdew, K. Burke, M. Ernzerhof, Phys. Rev. Lett. **77**, 3865 (1996).

438

[30] M. Gajdoš, K. Hummer, G. Kresse, Phys. Rev. B **73**,   (2006).

[31] Y. Z. Wang, B. L. Wang, Q. F. Zhang, R. Huang, B. L. Gao, F. J. Kong, X. Q. Wang, Chalcogenide Lett. **11**, 493 (2014).